Simulation of terahertz generation in corrugated plasma waveguides

Andrew J. Pearson, John Palastro, and Thomas M. Antonsen
Institute for Research in Electronics and Applied Physics, University of Maryland, College Park, Maryland 20742, USA
(Received 10 December 2010; published 25 May 2011)

We simulate the response of a corrugated plasma channel to an ultrashort laser pulse in two dimensions with the goal of demonstrating the production of terahertz frequency electromagnetic modes. Corrugated channels support electromagnetic modes that have a Floquet-type dispersion relation and thus consist of a sum of spatial harmonics with subluminal phase velocities. This allows the possibility of phase matching between the ponderomotive potential associated with the laser pulse and the electromagnetic modes of the channel. Since the bandwidth of an ultrashort pulse includes terahertz frequencies, significant excitation of terahertz radiation is possible. Here we consider realistic density profiles to obtain predictions of the terahertz power output and mode structure for a channel with periodic boundary conditions. We then estimate pulse depletion effects from our simulation results. The fraction of laser energy converted to terahertz is independent of laser pulse energy in the linear regime, and we find it to be around 1% . Extrapolating to a pulse energy of 0.5 J gives a terahertz power output of 6 mJ with a pulse depletion length of less than 20 cm.

DOI: 10.1103/PhysRevE.83.056403 PACS number(s): 52.38.−r

I. INTRODUCTION

Terahertz radiation lies between microwaves and infrared in the frequency spectrum. The wide variety of possible applications utilizing terahertz radiation, from spectroscopy and biological imaging to national security, medicine, and industry, make the development of small-scale terahertz devices critical. Today there exists a variety of terahertz sources, many of which are available commercially. Small-scale sources include far-infrared [1] and quantum cascade lasers [2], laser-driven terahertz antennae [3,4] and crystals [5], and backward wave oscillators [6]. In general, bright terahertz sources are based on free-electron devices, for example, gyrotrons [7] and free-electron lasers [8–10]. These can be large and relatively expensive to operate, and research into new terahertz sources continues [11].

Terahertz radiation generation by laser pulses in plasmas was first demonstrated by Hamster *et al*. [12]. The source of this radiation is the current driven by the ponderomotive force of a laser pulse or electron beam. In order for this current to couple to one or more electromagnetic modes of the plasma, the plasma density must be inhomogeneous, or there must be a strong background magnetic field [13]. The transfer of energy from a driver to terahertz radiation is limited by the fact that electromagnetic modes in a uniform plasma have superluminal phase velocities and so will quickly fall out of phase with the generated current, which travels with the driver at its group velocity.

Antonsen *et al*. [14] have suggested recently that a laser pulse passing through a plasma channel with an axially periodic density may generate terahertz radiation. As well as being inhomogeneous, these corrugated channels support electromagnetic modes that have a Floquet-type dispersion relation. This means that a mode in this channel consists of a sum of spatial harmonics, and many of these harmonics have subluminal phase velocities, thus allowing phase matching to occur between the driver and a mode.

In this paper we report the results of simulations of the generation of terahertz radiation in a corrugated plasma channel with realistic density profiles. These channels may be produced reliably in the laboratory [15] by line-focusing a laser pulse onto a cluster jet, as shown in Fig. 1(a). The periodic density structure is produced by spatial modulation of either the cluster density or the laser intensity. A second laser pulse (or possibly an electron beam) that follows the channel formation pulse serves as the driver for terahertz radiation.

This paper is organized as follows: In Sec. II we discuss the excitation and structure of electromagnetic modes in a corrugated channel. In Sec. III we give details of the code used to simulate the plasma response of the channel and present test results that verify the correct operation of the code. In Sec. IV we present and discuss results obtained for realistic system parameters. In Sec. V we present our conclusions.

II. EXCITATION OF MODES IN A CORRUGATED CHANNEL

A. Requirements for excitation

Our goal is to generate terahertz radiation by passing a laser pulse through a corrugated plasma channel. Since the central frequency of the pump pulse will be significantly larger than the terahertz frequencies, we can consider the cycle-averaged current generated by the ponderomotive force of the pulse as the source of the terahertz. Because of the periodicity of the channel, a component of this current will be associated with one or more electromagnetic modes. The frequency of these modes will be determined by the plasma frequency and other channel parameters.

There are two requirements that must be met in order to successfully generate electromagnetic radiation in a plasma using a laser pulse. Foremost is the requirement that energy must be transferred from the laser pulse to the plasma. The work done by the ponderomotive force on a current is

$$P = \frac{1}{e}\int d^3x \nabla V_p \cdot \boldsymbol{J} = -\int d^3x\, V_p \frac{\partial n}{\partial t}, \qquad (1)$$

where V_p is the ponderomotive potential, $\boldsymbol{J}$ is the current, e is the charge on an electron, and n is the number density of electrons. For power to be transferred from the laser pulse to a

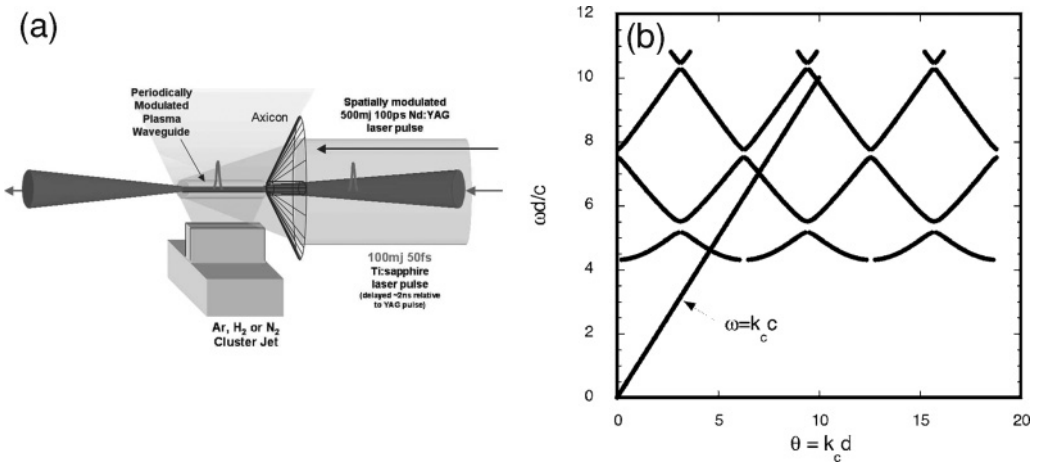

FIG. 1. (a) Diagram of experimental setup for producing a corrugated plasma channel [14,15]. As an alternative to a spatially modulated formation pulse, a modulated cluster density may be used in conjunction with a uniform formation pulse. (b) Dispersion plot of EM modes in the δ-function corrugated channel (considered by Antonsen *et al.* [14]), which consists of a channel with a density profile that has a train of δ functions, thus creating a period system while allowing the use of analytic results from the axially uniform case. Here, d is the distance between consecutive δ functions, while ω and k_c are the frequency and wavenumber, respectively.

mode of the plasma, this mode must have a density perturbation associated with it, i.e., the mode must have nonzero electric field divergence. For electromagnetic modes in a cold, linear fluid plasma, the divergence is of order

$$\nabla \cdot \boldsymbol{E} \sim O\left(\frac{\omega_p^2}{\omega^2-\omega_p^2}\frac{|\boldsymbol{E}|}{L}\right), \tag{2}$$

where ω is the mode frequency, ω_p is the plasma frequency, and L is the characteristic scale length of the nonuniformity of the plasma. For $L \to \infty$, the plasma becomes uniform and we recover the familiar result, $\nabla \cdot \boldsymbol{E} = 0$.

The second requirement is that the group velocity of the laser pulse is phase matched with the phase velocity of the excited modes. This is required for significant excitation to occur and is achieved in a corrugated channel because the electromagnetic modes of the channel are Floquet-type modes. Each mode of the channel consists of a sum over spatial harmonics, with the wavenumber of each harmonic separated by the wavenumber associated with the density modulations. Thus a plot of the dispersion relation [see Fig. 1(b)] demonstrates the periodicity in k space characteristic of waves in periodic systems and the presence of frequency band gaps in which no mode may propagate. The laser pulse, represented in the figure by a light line, is phase matched to the mode at several different frequencies. Maximal excitation occurs at these frequencies.

B. Parabolic plasma channels

In this paper we consider cylindrically symmetric corrugated waveguides with densities of the form

$$\frac{n(r,z)}{n_0} = \begin{cases} 1+\delta\sin(k_m z)+\dfrac{1}{2}\dfrac{r^2}{r_{\rm ch}^2} & r \leqslant r_c \\ \dfrac{n(r_c,z)}{n_0}\dfrac{r_0-r}{r_0-r_c} & r_c < r < r_0 \\ 0 & r \geqslant r_0 \end{cases} \tag{3}$$

Here, n_0 is the on-axis average density, δ is the density modulation amplitude, k_m is the wavenumber of the density modulations, $r_{\rm ch}$ the channel "width" that characterizes the density increase with radius, r_c the radius at which the linear "cutoff function" in the second line begins, and r_0 is the radius at which the density is zero.

In Sec. III we present numerical solutions to Maxwell's equations and the linear fluid equations for TM modes in plasma channels of this form. Before doing so, we use a number of approximations to explore this system analytically. In a cold, nonrelativistic and linearly responding plasma, an electromagnetic mode with small but nonzero electric field divergence and field components (E_r, B_θ, E_z) satisfies the approximate wave equation

$$\left(-\frac{1}{c^2}\frac{\partial^2}{\partial t^2}+\frac{\partial^2}{\partial z^2}+\frac{1}{r}\frac{\partial}{\partial r}r\frac{\partial}{\partial r}-\frac{1}{r^2}\right)E_r = \frac{\omega_{p0}^2}{c^2}\frac{n(r,z)}{n_0}E_r, \tag{4}$$

where ω_{p0} is the plasma frequency evaluated for the density n_0.

In the case $r_c \to \infty$, only the first part of Eq. (3) is relevant and we have a so-called parabolic plasma channel, albeit with axial density modulations. The r and z dependence in this density profile are separable, allowing an analytic solution. In axially uniform channels ($\delta = 0$), we recover the wave equation for modes in a regular parabolic plasma channel. The solution is harmonic in z and consists of a linear combination of radial eigenmodes, of which there are an infinite number. The solution to Eq. (4) for the fundamental radial eigenmode is

$$E_r(r,z,t) = E_0 e^{i(k_z z-\omega t)}\frac{r}{w_{\rm ch}}e^{-r^2/w_{\rm ch}^2}. \tag{5}$$

Here, $w_{\rm ch}$ is the mode width given by $8/w_{\rm ch}^4 = (\omega_{p0}^2/r_{\rm ch}^2c^2)$. The dispersion relation is

$$\omega^2 = \omega_{p0}^2 + k_z^2c^2 + \frac{8c^2}{w_{\rm ch}^2}. \tag{6}$$

When we include axial modulations ($\delta \neq 0$), applying separation of variables to Eq. (4) yields the same ordinary differential equation (ODE) in r as for the axially uniform case, and so the ansatz for E_r becomes

$$E_r(r,z,t) = E_0 e^{-i\omega t} f(z) \frac{r}{w_{\rm ch}} e^{-r^2/w_{\rm ch}^2}. \tag{7}$$

The dispersion relation is now

$$\omega^2 = \omega_{p0}^2 + k_0^2 c^2 + \frac{8c^2}{w_{\rm ch}^2}, \tag{8}$$

where k_0 is the separation-of-variables parameter. This features in the ODE for $f(z)$

$$\frac{d^2 f}{dz^2} + k_0^2 f = \frac{\omega_{p0}^2}{c^2} \delta \sin(k_m z) f. \tag{9}$$

This is the Mathieu equation, and as such cannot be solved analytically. We know from Floquet's theorem, however, that the solution must be of the form

$$f(z) = e^{ik_z z} \sum_{\alpha=-\infty}^{\infty} A_\alpha e^{-i\alpha k_m z}. \tag{10}$$

This solution implies a relation $k_z = k_z(k_0)$, and by inversion $\omega = \omega(k_z)$. In general, all coefficients A_α are nonzero and cannot be found except by infinite recursion.

By substituting Eq. (10) into Eq. (9), we recover

$$\left[k_0^2 - (k_z - \alpha k_m)^2\right] A_\alpha = \frac{\omega_{p0}^2}{c^2} \frac{\delta}{2i} [A_{\alpha-1} - A_{\alpha+1}]. \tag{11}$$

In the limit $\delta \to 0$, we have $k_0 = k_z - \alpha k_m$ for the harmonic with Fourier coefficient A_α. This is reconciled with the axially uniform solution $k_0 = k_z$ by noting that in this case, $A_\alpha = 0$ for all $\alpha \neq 0$. We construct an approximate dispersion relation for small δ by using the $\delta \to 0$ solution and superimposing on an ω-k_z plot an infinite set of functions of the form

$$\omega = \sqrt{\omega_c^2 + (k_z - \alpha k_m)^2 c^2} \qquad \alpha \in \mathbb{Z}, \tag{12}$$

where $\omega_c^2 = \omega_{p0}^2 + 8c^2\gamma/w_{\rm ch}^2$ (γ is the radial eigenmode number). This set of curves deviates from the true dispersion relation near the intersections. At these points, the true dispersion relation will exhibit band gaps in which no propagating wave solution exists. Away from these points, and depending on system parameters, Eq. (12) will be a good approximation to the true dispersion relation. A discussion of this, including more accurate calculations of the dispersion relation, is found in the Appendix.

An excited mode in this channel consists of a sum of spatial harmonics, each harmonic corresponding to a different value of α. The laser pulse traveling at group velocity $v_g \simeq c$ phase matches one of these harmonics, which results in the excitation of a mode. As seen in Fig. 1(b), this excitation occurs at frequencies given by the intersection points between the lightline of the laser pulse and the dispersion curves. Replacing k_z with ω/c in Eq. (12) gives us the following estimate for the frequencies of the excited modes:

$$\omega = \frac{1}{2\alpha k_m c}\left(\omega_c^2 + \alpha^2 k_m^2 c^2\right) \qquad \alpha = 1,2,\ldots . \tag{13}$$

We refer to modes excited in this way as Floquet modes. Thus for each radial eigenmode there is a spectrum of Floquet modes generated with frequencies given by Eq. (13). We reinforce here that Eq. (13) is only strictly valid in the small-δ limit and the calculated frequencies are only accurate away from the intersections, which indicate the positions of band gaps in the exact dispersion relation. We note that depending on the choice of modulation period, $\alpha = 1$ does not necessarily label the lowest excited frequency; this is just a peculiarity of the notation.

C. Finite radius plasma channels

In this work we do not consider true parabolic plasma channels (i.e., with $n \to \infty$ as $r \to \infty$) beyond the discussion in this section, because the corrugated plasma channels produced in the laboratory have a density maximum at a finite radius followed by a decrease to zero density [as described by Eq. (3)]. We conclude this section with a brief discussion of two relevant differences between finite-radius channels and parabolic plasma channels.

The first difference is the fact that finite radius channels support a finite number of modes, unlike parabolic plasma channels which support a denumerably infinite number of radial eigenmodes. To estimate the number of modes a channel will support, we consider the local dispersion relation for an axially smooth parabolic channel:

$$\omega^2 = \omega_{p0}^2\left(1 + \frac{r^2}{2r_{\rm ch}^2}\right) + k_z^2 c^2 + k_\perp^2 c^2. \tag{14}$$

If the finite channel supports Γ modes, then we assume that the dispersion relation for these modes is similar to that for the first Γ modes of the parabolic channel, i.e.,

$$\omega^2 = \omega_{p0}^2 + k_z^2 c^2 + \frac{8\gamma c^2}{w_{\rm ch}^2} \qquad \gamma = 1 \ldots \Gamma. \tag{15}$$

By combining these two equations and using the relationship between $r_{\rm ch}$ and $w_{\rm ch}$ described in this section, we obtain a simple expression for the perpendicular wavenumber:

$$k_\perp^2 = \frac{4}{w_{\rm ch}^2}\left(2\gamma - \frac{r^2}{w_{\rm ch}^2}\right). \tag{16}$$

A mode is bound if the perpendicular wavenumber passes through zero at some radius, and so if the density maximum in the channel exists at radius r_c, modes for which $\sqrt{2\gamma} < r_c/w_{\rm ch}$ will be bound. Alternatively, the number of bound modes is

$$\Gamma = \texttt{int}\left(r_c^2/2w_{\rm ch}^2\right) \tag{17}$$

The second difference is that the energy in an EM mode may leak through the channel wall and couple to vacuum electromagnetic modes. Thus an excitation propagating down the channel will deplete in a finite distance. Of course, this is true for both a laser pulse propagating down a channel

(and thus losing energy that may otherwise be converted to terahertz) and terahertz modes excited by the pulse. A WKB treatment of this effect for a smooth channel may be found in [16]. The rate at which depletion occurs is governed by the transmission coefficient, which in general depends on the height and thickness of the wall of the channel. In the next section this effect is considered numerically for channels described by Eq. (3).

III. CODE DETAILS AND VERIFICATION

A. Model and assumptions

The main purpose of this paper is to describe a series of simulations carried out to determine the characteristics of the terahertz radiation emission from a corrugated plasma channel. The terahertz radiation is the result of currents generated by the ponderomotive force of the laser pulse. For both linearly and radially polarized pulses, the ponderomotive force is cylindrically symmetric, which we expect the terahertz modes to be TM modes consisting of components E_r, B_θ, and E_z, which satisfy Maxwell's equations:

$$\begin{aligned} \frac{1}{c}\frac{\partial E_r}{\partial t} &= -\frac{4\pi J_r}{c} - \frac{\partial B_\theta}{\partial z} \\ \frac{1}{c}\frac{\partial E_z}{\partial t} &= -\frac{4\pi J_z}{c} + \frac{1}{r}\frac{\partial}{\partial r}(r B_\theta) \\ \frac{1}{c}\frac{\partial B_\theta}{\partial t} &= \frac{\partial E_z}{\partial r} - \frac{\partial E_r}{\partial z}. \end{aligned} \tag{18}$$

The current components J_r and J_z must be calculated by determining the plasma response to the the ponderomotive force of the laser pulse and the field components determined by the above equations. We do so by modeling the plasma as a linear, nonrelativistic, cold electron fluid with a fixed ion background. The evolution of the current $\boldsymbol{J} = -en_0(r,z)\boldsymbol{v}$, where the density $n_0(r,z)$ is given by Eq. (3), is determined by solving the momentum equation

$$m_e\frac{\partial \boldsymbol{v}}{\partial t} \simeq -e\boldsymbol{E} - \nabla V_p - \nu m_e \boldsymbol{v}, \tag{19}$$

where ν is a collisional damping factor and V_p is the ponderomotive potential of the laser pulse. This is typically written as

$$V_p(r,z,t) = \frac{m_e c^2}{2}|\boldsymbol{a}(r,z,t)|^2, \tag{20}$$

where $\boldsymbol{a}(r,z,t)$ is the normalized vector potential of the laser pulse. In this work we consider the laser pulse to be propagating but nonevolving, and so the ponderomotive potential is simply a known function of r and $z - v_g t$ that is substituted into Eq. (19). We use a potential of the form

$$\begin{aligned} V_p(r,z-ct) &= V_{p0}e^{-2r^2/w_{\rm ch}^2}\cos^4\left(\pi\frac{z-ct}{c\tau}\right) \\ &-\frac{c\tau}{2} \leqslant z - ct \leqslant \frac{c\tau}{2}, \end{aligned} \tag{21}$$

where τ is the laser pulse duration.

There are conditions that must be satisfied if the system is to be modeled accurately in the manner described above. To begin, the ponderomotive potential must be sufficiently small that both the quiver velocity of the electrons and their cycle averaged motion is nonrelativistic. While we do not simulate behavior on the optical time scale, the size of the ponderomotive potential is related to the laser frequency and electric field amplitude, hence the relevance of this condition. The inequality that must hold for both of these conditions to be satisfied is

$$\frac{V_{p0}}{m_e c^2} = \frac{1}{2}|\boldsymbol{a}_0|^2 \ll 1, \tag{22}$$

where a subscript zero indicates a peak value.

Next, we consider the cold fluid limit. For the plasma to be considered cold, there must be insufficient time for the fluid to thermalize on the time scale of the electron oscillations. This is expressed simply through the inequality

$$k v_{\rm th} \ll \omega, \tag{23}$$

where $v_{\rm th} \sim \sqrt{k_B T/m_e}$ is the thermal electron velocity and ω and k are a typical frequency and wavenumber of terahertz radiation. Since the terahertz is generated by a pulse moving at $v_g \simeq c$ we expect $\omega/k \sim v_g$, and Eq. (23) should be satisfied.

To determine whether we may treat the ions as a fixed, neutralizing background, we must compare the time scale of the laser pulse to the inverse of the ion plasma frequency. Since we are interested in generating radiation in the terahertz regime, our laser pulse must be short enough that the bandwidth of its envelope encompasses the desired terahertz frequencies. Moreover, the amplitude of the pulse shape in frequency space must be large at the desired frequencies. In order to generate radiation in the range 1–10 THz, our laser bandwidth must be of the order of hundreds of terahertz, which means we must consider pulse durations of less than 100 fs. By comparison, the inverse ion plasma frequency is 750 fs at $n_0 \sim 1\times10^{18}$ cm^{-3} and 7.5 ps at $n_0 \sim 1\times10^{16}$ cm^{-3}. Since the inverse ion plasma frequency represents the shortest time scale of ion motion, we conclude that if we restrict ourselves to sufficiently short pulses and sufficiently low densities, we may consider the ions as being stationary.

Finally we consider the validity of the assumption that the laser pulse is nonevolving. This is potentially a stringent approximation, and importantly, we must consider two regimes of validity in dealing with the simulation results. In the first regime the approximation is valid if the pulse does not change shape or amplitude significantly over the length of the simulation window, which will be on the order of tens of density modulations, or a few millimeters. In this case, quantities measured over this distance for a nonevolving laser pulse will match those that would be measured for an evolving laser pulse. We may then estimate the pulse depletion length by writing down the following energy-conservation expression:

$$\frac{1}{U_L^2}\frac{dU_L}{dt} = \frac{P}{U_L^2} \simeq \frac{\langle P_T\rangle}{U_0^2}. \tag{24}$$

Here, $U_L(t)$ is the energy in an evolving pulse, $P(t)$ is the power transferred to plasma currents by an evolving pulse, $U_0 = U_L(0)$ is both the initial energy of an evolving pulse and the energy of a nonevolving pulse in our simulation, and $\langle P_T\rangle$ is the average power transferred to the plasma by a nonevolving pulse of energy U_0.

In the linear regime the pulse energy $U_L(t)$ scales as V_p, and power $P(t)$ lost from the pulse scales as V_p^2. If we assume that

the pulse shape does not change significantly over the depletion length, then the middle part of Eq. (24) is approximately constant. If we are within the first regime of validity, we may estimate the value of this constant using the right-hand side. Then the solution to Eq. (24) is

$$\frac{U_L(t)}{U_0} = \left(1 + \frac{\langle P_T\rangle t}{U_0}\right)^{-1}. \tag{25}$$

Here we identify the depletion length of the pulse $L_D = cU_0/\langle P_T\rangle$.

The second regime of validity concerns whether or not the above depletion estimate is accurate. The concern is due to pulse evolution effects that occur on scale lengths longer than the simulation length but shorter than the estimated depletion length. These can be both linear shape evolution effects, such as group velocity dispersion, and nonlinear evolution effects, such as pulse compression due to density-perturbation-induced group velocity variation, and redshifting due to phase velocity variation [17]. We note that within our model, L_D scales inversely with pulse energy, and results for different pulse energies can be found by rescaling the result of a single run with a reference pulse energy. Therefore we must consider the validity of the approximation for both the depletion length obtained from our simulation results and for depletion lengths obtained through rescaling our results. Conflicts in this area are discussed when we present rescaled depletion estimates in Sec. IV.

Returning to the first regime of validity, there are several pulse evolution effects to consider. First we consider pulse depletion due to plasma wake excitation. In an axially uniform plasma, this is maximized when the pulse length matches the wavelength of the plasma oscillations. For plasma densities of 5×10^{17} to 2.5×10^{18} cm^{-3}, this occurs for pulse lengths of 160–70 fs, respectively. The depletion length for a pulse initially at linear resonance in the weakly relativistic regime ($a_0^2 \ll 1$) is given by [17,18]

$$k_p L_{dp} \simeq \frac{17.4}{a_0^2}\left(\frac{k_0}{k_p}\right)^2, \tag{26}$$

where k_0 is the central wavenumber of the laser pulse and $k_p = \omega_{p0}/c$. For a laser energy of 0.01 J, wavelength of 800 nm, and pulse width of 15 μm ($a_0 \simeq 0.1$), the depletion lengths for the given density range go from about 3300 to 300 cm. For a laser energy of 0.5 J ($a_0 \simeq 0.8$), which is the energy to which we intend to rescale our results, the depletion lengths range from around 70 to 6 cm. We note that this is the depletion length for a pulse with initial length equal to the plasma wavelength. Our pulse is somewhat shorter than the ambient plasma wavelength, and since the plasma wavelength in our simulation changes because of the density modulations, the pulse spends some time even further away from resonance. Hence we expect the pulse depletion length in a modulated channel to be larger than that predicted by Eq. (26).

Another effect to consider is group velocity dispersion (GVD). This effect may be estimated by considering the range of group velocities in a pulse of length $c\tau$ in configuration space and its corresponding length in Fourier space [19]. The propagation distance over which the pulse doubles in length is given by

$$L_{GVD} \simeq k_0 c^2 \tau^2 \left(\frac{k_0}{k_p}\right)^2. \tag{27}$$

For our given density range, L_{GVD} ranges from about 600 to 100 cm, which is significantly longer than the simulation length.

Although GVD happens relatively slowly, the pulse may still disperse due to the Floquet structure of the EM modes in our system. The laser pulse is composed of Floquet modes, meaning that each mode consists of a set of spatial harmonics. For any given mode the group velocity of each spatial harmonic is the same; however, if the bandwidth of the pulse overlaps a band gap, some of the modes will have significantly different group velocities than they would in a pulse traveling in a uniform channel, leading to rapid pulse deformation.

This, however, is not an issue in our system. The pulse bandwidth extends over several band gaps, which at high frequency are separated by $\omega \simeq k_m c/2$. The band gaps themselves, however, have essentially zero width in the high-frequency regime. This may be seen by referring to the calculation performed in the Appendix, the relevant results of which are displayed in Fig. 2. Note that the frequency at which the band-gap size vanishes is significantly lower than the laser frequency, and hence the approximate dispersion relation in Eq. (12) becomes exact in the high-frequency limit.

Our conclusion, therefore, is that although an optical-frequency pulse in a corrugated system will be composed of modes consisting of several spatial harmonics, the dispersion structure of each of the harmonics in a mode will be the same (up to a k offset) as those of the corresponding mode from a pulse in an axially uniform channel.

In order to reinforce the validity of the nonevolving pulse approximation, we perform simulations with the code WAKE [20] using our channel parameters over many Rayleigh lengths. Plots (a)–(c) of Fig. 3 show the Fourier transforms of the pulse envelope from such a simulation, conducted for a modulated plasma channel with central density $n_0 = 10^{18}$ cm^{-3},

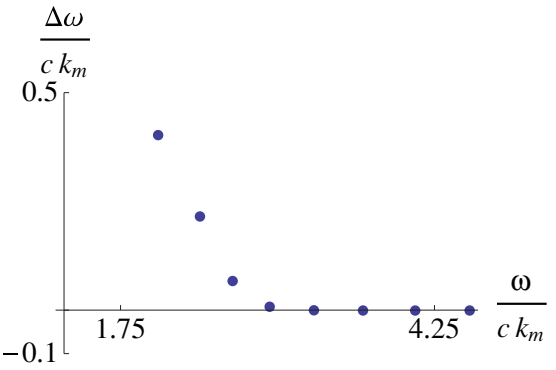

FIG. 2. (Color online) Plot of normalized band-gap size as a function of normalized central band-gap frequency, obtained from the numerical calculation of the dispersion relation, performed in the Appendix. Note that the band-gap size vanishes rapidly with increasing frequency, at a point far below the typical frequencies associated with an optical pulse.

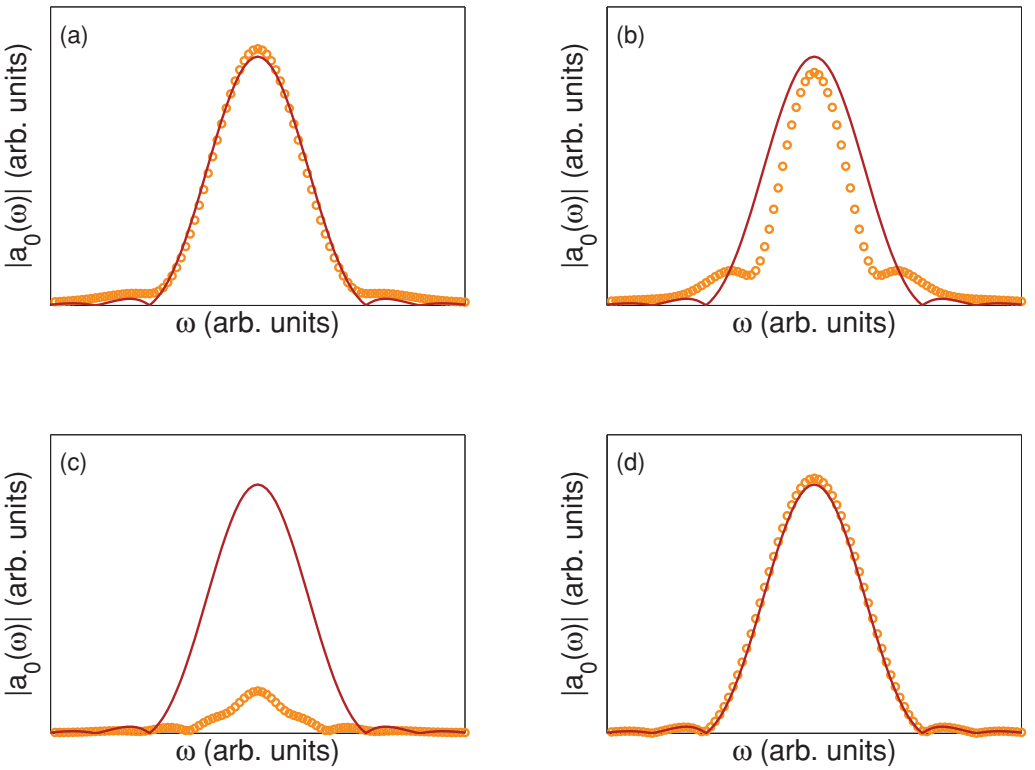

FIG. 3. (Color online) Plots of the Fourier transforms of 50-fs laser pulses with wavelength 800 nm and spot size 15 μm, recorded initially (red, solid) and after (orange, circles) propagation for 40 Rayleigh lengths for normalized vector potential amplitudes of (a) $a_0 = 0.2$, (b) $a_0 = 0.4$, and (c) $a_0 = 0.8$. These potentials correspond to pulse energies of 0.03, 0.1, and 0.5 J, respectively. Plot (d) is for $a_0 = 0.8$ for a pulse propagating over one Rayleigh length. These plots were generated using the simulation WAKE [20].

modulation amplitude $\delta = 0.9$, and modulation wavelength 50 μm for a pulse of length 50 fs, width 15 μm, wavelength 800 nm, and normalized vector potential amplitudes of $a_0 = 0.2$, $a_0 = 0.4$, and $a_0 = 0.8$. As can be seen from the plots, the frequency content of the weakest pulse changes little over a length of 40 Rayleigh lengths, which corresponds to about 15 cm for a 15-μm-width pulse. Such a pulse is consistent with the first regime of validity. Over this length, the frequency content of a stronger pulse changes significantly. In Fig. 3(b) there appears to be some pulse broadening, whereas in Fig. 3(c), significant pulse depletion has occurred. In Fig. 3(d) we see that the frequency content of even a strong pulse changes little over one Rayleigh length, and so it is marginally consistent with the first regime of validity.

From the preceding discussion we conclude that we can obtain useful results from our model. In particular, the first regime of validity of the nonevolving approximation holds over a wide range of parameters. Care must be taken when using the results to obtain estimates of the depletion length, since violations of the second regime of validity may occur. In the case of low-energy pulses, the depletion length L_D often exceeds the group velocity dispersion length L_{GVD}, while in the case of high-energy pulses, significant changes in pulse shape occur despite the the depletion length being much shorter. In this discussion we have neglected instabilities (such as the Raman instability) that cause the pulse shape to change. These can be ignored for a 50-fs laser pulse, and we consider any effect they may have as a subject for future study.

B. Algorithm

The fact that the plasma responds in a linear fashion allows us to use a simple algorithm to simulate the time evolution of the fields and currents. The electric and magnetic field components are solved on a two-dimensional Yee grid as follows:

$$\begin{aligned}
\frac{[E_r]^{n+(1/2)}_{i,j+(1/2)} - [E_r]^{n-(1/2)}_{i,j+(1/2)}}{c\Delta t} &= -\frac{4\pi [J_r]^n_{i,j+(1/2)}}{c} \\
&\quad - \frac{[B_\theta]^n_{i,j+1} - [B_\theta]^n_{i,j}}{\Delta z} \\
\frac{[E_z]^{n+(1/2)}_{i+(1/2),j} - [E_z]^{n-(1/2)}_{i+(1/2),j}}{c\Delta t} &= -\frac{4\pi [J_z]^n_{i+(1/2),j}}{c} \\
&\quad + \frac{(i+1)[B_\theta]^n_{i+1,j} - i[B_\theta]^n_{i,j}}{[i+(1/2)]\Delta r} \\
\frac{[B_\theta]^{n+1}_{i,j} - [B_\theta]^n_{i,j}}{c\Delta t} &= \frac{[E_z]^{n+(1/2)}_{i+(1/2),j} - [E_z]^{n+(1/2)}_{i-(1/2),j}}{\Delta r} \\
&\quad - \frac{[E_r]^{n+(1/2)}_{i,j+(1/2)} - [E_r]^{n+(1/2)}_{i,j-(1/2)}}{\Delta z}.
\end{aligned} \tag{28}$$

Here, n is the time index, i is the radial index, and j is the axial index. The current is evaluated at integer time steps, and each component is evaluated on the spatial grid at the same location as the corresponding electric field component. This is possible because of the absence of the convective term in the

momentum equation, and because the ponderomotive force is a known function $V_p(r,z-v_g t)$ which can be evaluated at any point in space and time.

The damping term in Eq. (19) requires a manipulation to allow the evaluation of the current. Writing $\boldsymbol{v}^{n+(1/2)} = \frac{1}{2}(\boldsymbol{v}^n + \boldsymbol{v}^{n+1})$ and approximating the derivative as a central difference centered around $n+\frac{1}{2}$, we have

$$\left(1+\frac{\nu\Delta t}{2}\right)m_e\boldsymbol{v}^{n+1} = \left(1-\frac{\nu\Delta t}{2}\right)m_e\boldsymbol{v}^n - \Delta t\left(e\boldsymbol{E}^{n+(1/2)} + \nabla V_p^{n+(1/2)}\right). \tag{29}$$

From this, it is a simple matter to calculate the current components $[J_r]^n_{i,j+(1/2)}$ and $[J_z]^n_{i+(1/2),j}$ via $\boldsymbol{J} = -en_0(r,z)\boldsymbol{v}$.

C. Postprocessing

We implement this algorithm using the relatively new NVidia Tesla General Purpose Graphical Processing Units [21] designed for use in desktop-scale parallel computation. During the simulation, we allow the laser pulse to pass through the system several times by using periodic boundary conditions in z, and on the first laser pulse "pass" we ramp V_{p0} from zero to full strength to eliminate transients. The collisional damping term in Eq. (19) is set so as to reduce the laser wake significantly after one laser pass, thus preventing overlap of the pulse with its wake from the previous pass. For these simulations, we use $\nu = 8c/L_S$, where L_S is the chosen system length. For a density of $n = 10^{18}$ cm^{-3} and a system length of 0.32 cm (both typical values), this is 1.3% of the plasma frequency.

We must also deal with radial boundary conditions. At the origin, these are $E_r = B_\theta = 0$ and $\partial E_z/\partial r = 0$, while all fields must vanish at infinity. Noting that the structure of the Yee cell means that we only need specify E_z and J_z at the boundaries, we choose the inner simulation boundary to be at $r = -\Delta r/2$ and set $[E_z]^{n+(1/2)}_{-(1/2),j} = [E_z]^{n+(1/2)}_{+(1/2),j}$ and $[J_z]^n_{-(1/2),j} = [J_z]^n_{+(1/2),j}$. For the outer boundary, we use a perfectly matched layer the size of two plasma wavelengths to ensure that any terahertz radiation that escapes the channel will not be reflected from the boundary.

Once the laser pulse has passed through the system several times, we must determine the amount of terahertz radiation emitted. On the last pass of the laser pulse, we store various field quantities for this purpose. We store for all z and t the r integral of the product of the radial part of the ponderomotive potential and the current divergence for the purpose of calculating the power transferred to the plasma by the laser pulse. We also store for all z and t the z component of the electric field and the magnetic field at a fixed radius R outside the channel for the purpose of calculating the radial Poynting flux, and for all r and t the r component of the electric field and the magnetic field at a fixed axial position Z for the purpose of calculating the radial Poynting flux.

Storing information about individual time steps allows us to calculate time-averaged quantities as sums in frequency space. Writing the ponderomotive potential as $V_p(r,z-ct) = V_{p0}g(z,t)h(r)$, we have

$$\begin{aligned}
\langle P_T\rangle &= \int \frac{d\omega}{2\pi}\, p_T \\
&= \int \frac{d\omega}{2\pi}\left[-\frac{2\pi V_{p0}}{eT} \times \int dz\, \tilde{g}(z,\omega)\int r dr\, h(r)\nabla\cdot\tilde{\boldsymbol{J}}(r,z,-\omega)\right] \\
\langle P_r\rangle &= \int \frac{d\omega}{2\pi}\, p_r \\
&= \int \frac{d\omega}{2\pi}\left[-\frac{c}{2T}\int R dz\, \tilde{E}_z(R,z,\omega)\tilde{B}_\theta(R,z,-\omega)\right] \\
\langle P_z\rangle &= \int \frac{d\omega}{2\pi}\, p_z \\
&= \int \frac{d\omega}{2\pi}\left[\frac{c}{2T}\int r dr\, \tilde{E}_r(r,Z,\omega)\tilde{B}_\theta(r,Z,-\omega)\right],
\end{aligned} \tag{30}$$

where tilde indicates a Fourier transform in time, and the quantities in brackets are power densities in frequency space. For the simulation, integrals are replaced by the appropriate sums and T is the duration of one laser pulse pass. Studying the power densities will reveal the frequencies of the excited modes. In addition to calculating these quantities, we may gain information about the spatial structure of the modes by looking at the Fourier transform in both z and t of the stored field quantities.

D. Code verification

Before using the code to generate results, we must ensure correct operation. We do this by comparing numerical results to analytic results and by verifying energy conservation in the small-stepsize limit. Various plots associated with the first stage of code verification are shown in Fig. 4.

Fig. 4(a) shows the linear density perturbation as a function of axial distance calculated analytically and numerically. In the simulation, the laser pulse is allowed to pass through the system several times before the density perturbation is recorded, and the small oscillations leading the pulse are the damped wake from the previous laser pass. Fig. 4(b) shows the quantity $\Delta P = \langle P_T\rangle - \langle P_L\rangle$ as a function of the square of the normalized time step, where $\langle P_L\rangle$ is the power extracted from the system due to the collisional damping term. The power difference ΔP varies linearly, as expected from the second-order numerical error associated with the chosen algorithm. It converges in the limit $dt \to 0$ to a value six orders of magnitude less than the individual power measurements; hence we conclude that in this case, our code displays the appropriate energy conservation properties.

In Figs. 4(c) and 4(d) we see Fourier transforms of E_z generated by a laser pulse in an axially uniform parabolic plasma channel. In both plots the horizontal line indicates the plasma frequency on axis, while the curved lines are the dispersion curves for the first three radial eigenmodes. In Fig. 4(c), the transform is taken on axis. There is a strong excitation at the plasma frequency, as evidenced by the peaks of $\tilde{E}_z(k_z,\omega)$ at the intersection of the light line and the plasma

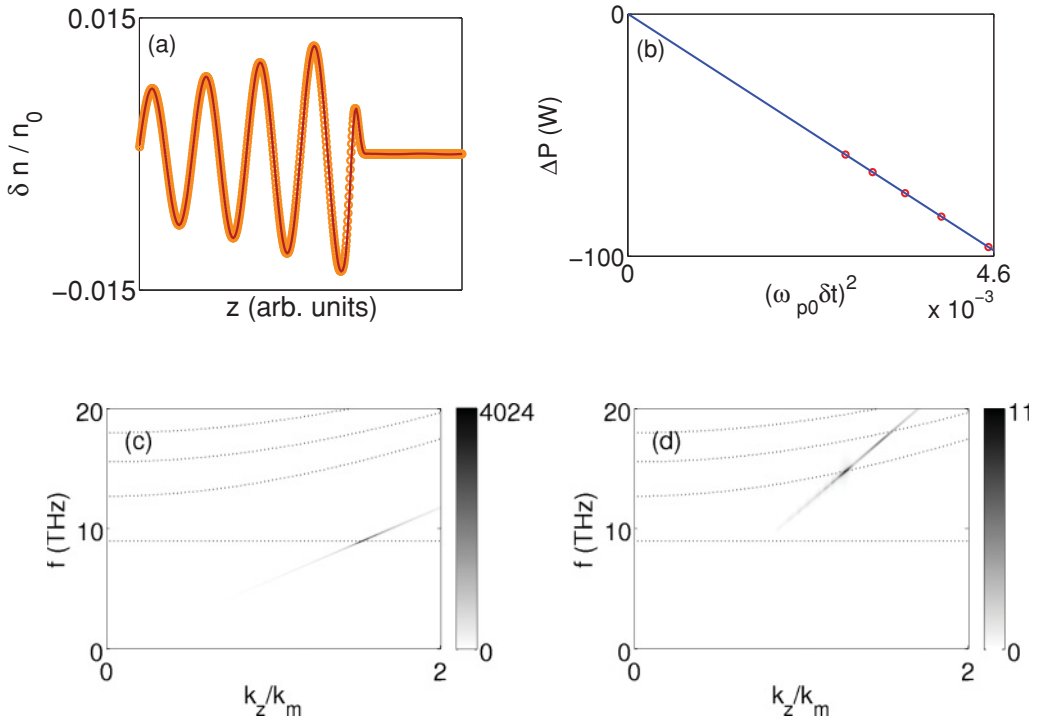

FIG. 4. (Color online) Plots from a simulation of a laser pulse passing through a uniform plasma showing (a) density perturbation $\delta n/n_0$ calculated analytically (red, solid) and numerically (orange, circles) for a uniform plasma and (b) difference between power input and output as a function of normalized stepsize squared. Plots of $\widetilde{E}_z(k_z,\omega)$ from a simulation of a laser pulse passing through a parabolic plasma channel evaluated for (c) $v_g = c$ at $r = 0$ and (d) for $v_g = 2c$ at $r > r_0$. The dotted blue lines are the dispersion curves for plasma waves and the first three radial eigenmodes.

frequency, which is consistent with the expectation that strong excitation requires phase matching.

In Fig. 4(d), the transform is taken at a radius outside the plasma channel and with the laser pulse group velocity set to $v_g = 2c$. While not physically realistic, this is possible in the code because the pulse is modeled as a force that depends on $z - v_g t$, where v_g is a free parameter. Here there are several excitations corresponding to the lowest frequency EM modes in the channel. There is no plasma wave excitation, since the density at the point of measurement is zero. While we match the laser pulse spot size to the fundamental mode width (which is a requirement if our nonevolving laser pulse assumption is to be valid), the ponderomotive force consists of a broad spectrum of radial eigenmodes. Since this is responsible for driving the current, we expect to see excitations above the fundamental.

Now we look at axial and radial average power outputs recorded for the cases of $\delta = 0$ and $\delta = 0.05$ in both radially uniform plasmas and finite radius plasma channels. We choose a density of $n_0 = 10^{18}$ cm^{-3}, 16 corrugations of length 50 μm and a laser pulse mode width of $w_{\rm ch} = 15$ μm. In the radially uniform case, the mode width does not carry its usual physical interpretation and is to be thought of as just a length scale. In all cases, we use a laser pulse with an energy of $U_L = 0.01$ J and we choose cutoff parameters $r_c = 2w_{\rm ch}$ and $r_0 = 3w_{\rm ch}$.

In Fig. 5(a), we see a very small excitation around the plasma frequency (which for our chosen density is 9.0 THz). This is to be expected, since in a uniform plasma we expect no EM excitation and plasma waves have no Poynting flux. In Fig. 5(b) we see much larger excitations. The radial Poynting flux is an EM mode, since the plasma density is zero at the point of measurement. The nature of the axial excitations is not clear, since in a channel with nonuniform density the magnetic fields generated by the plasma wave currents do not sum to zero. In these simulations, however, the axial Poynting flux is of less importance than the radial Poynting flux. This is because the periodic boundary conditions make our channel infinite in length, and so even if we could isolate the contribution to the axial flux from EM modes, the recorded value would not be an accurate representation of the amount of terahertz exiting the end of a finite-length waveguide.

In Fig. 5(c) we again see an excitation in the axial power flow plot. There is no significant excitation in the radial plot, consistent with $\delta = 0$. In Fig. 5(d) we see excitations between 10 and 20 THz in the radial power flow plot. For comparison, the first seven predicted Floquet frequencies for the fundamental radial eigenmode are 12.7, 13.5, 15.4, 16.4, 17.7, 20.2, and 22.9 THz. We note that a much smaller amount of radiation escapes radially than in the case of Fig. 5(b). This is because the generated modes are unbound and have a Rayleigh length much shorter than the simulation length.

Finally, we study the power balance in the four scenarios in Fig. 5. The results are listed in Table I. In the case of Figs. 5(a), 5(c), and 5(d), we see that the different measures produce somewhat different results. This is of no concern, however, since the ΔP results are six orders of magnitude less than their respective values of $\langle P_T \rangle$ and $\langle P_L \rangle$ and are probably influenced by floating point error. Accordingly, the result for

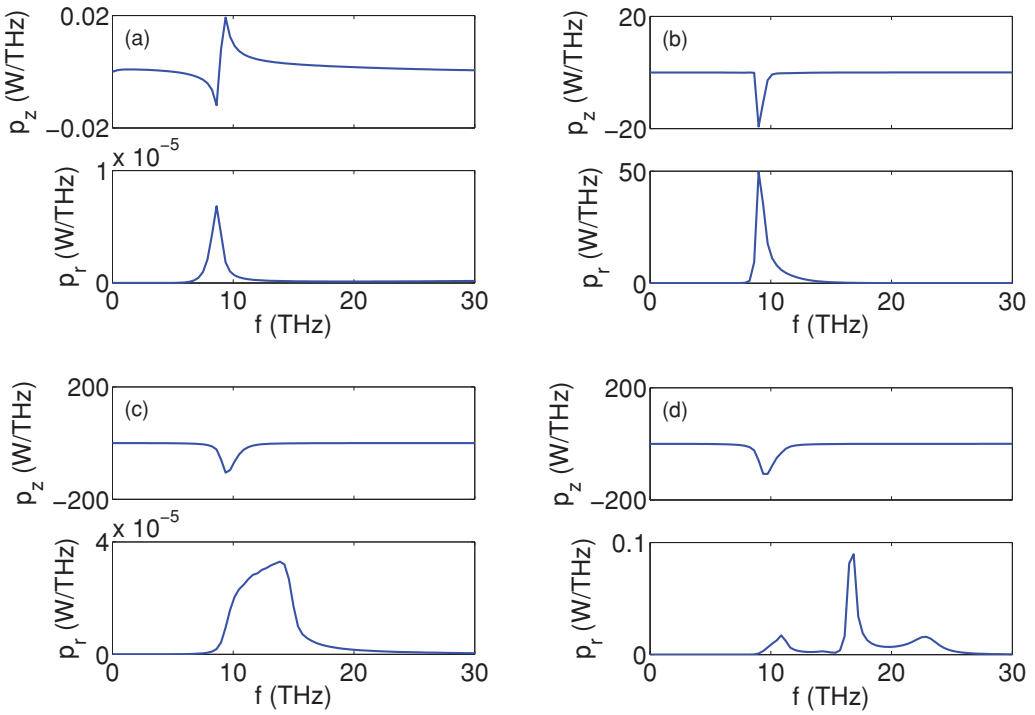

FIG. 5. (Color online) Axial and radial power flow density in frequency space for (a) uniform plasma, (b) $\delta = 0.05$ axial corrugations but no radial density dependence, (c) a finite radius plasma channel with no axial corrugations, and (d) a finite radius plasma channel with $\delta = 0.05$ axial corrugations.

Fig. 5(b) is much more accurate. A similar level of accuracy is demonstrated in the last row of the table, in which we record the results for a "full-strength" corrugated channel of the type that will be studied in the next section.

IV. SIMULATION RESULTS

We begin by presenting results for the total power output calculated from the simulation for various densities and laser spot sizes. Fig. 6 contains the average radial power exiting the side of the waveguide as well as the average axial power flow, the percentage of laser energy converted to terahertz, and the average angle of emission. These results are recorded for a range of densities and mode widths, for a laser pulse energy $U_0 = 0.01$ J, modulation amplitude $\delta = 0.9$, and density cutoff parameters $r_c = 2w_{\rm ch}$ and $r_0 = 3w_{\rm ch}$. The pulse length is 50 fs, and the optical wavelength (which is used in conjunction with U_0 to determine the peak ponderomotive potential) is 800 nm.

TABLE I. Values of the difference between power input and output ΔP and the radial power flow $\langle P_r \rangle$ for the different scenarios in Fig. 5. For comparison, the result for a full-strength ($\delta = 0.9$) channel is listed.

Figure	$\lim_{\Delta t \to 0} \Delta P$ (W)	$\lim_{\Delta t \to 0} \langle P_r \rangle$ (W)
5(a)	0.117	0.000 164
5(b)	306	305
5(c)	0.0930	0.000 276
5(d)	1.47	0.404
$\delta = 0.9$	475	472

The density modulation period is 50 μm and the total system length is 0.32 cm.

In Fig. 6(a) we see the radial power flow as a function of average on-axis density, measured for several different mode widths. We see that the largest terahertz generation occurs for small mode widths. In general, this occurs because we have kept the energy content of the pulse fixed, and so the peak ponderomotive potential is larger in the case of smaller mode width. The amount of terahertz produced increases with density, because the work done on the plasma by the laser pulse is larger for larger density.

In Fig. 6(b) we see the axial power flow as a function of average on-axis density, measured for several different mode widths. This quantity may take a negative value, since the mode may propagate either way along the channel. Backward-propagating waves come from lightline intersections with the dispersion function when its gradient is negative. We see that the axial flow is typically several times smaller than the radial flow, which is a desirable property because of the difficulties in calculating accurately the terahertz output from the end of a real channel.

In Fig. 6(c) we plot the ratio of $\langle P_r \rangle$ to $\langle P_T \rangle$ as a percentage, which serves as an estimate of the fraction f of laser energy that is converted to terahertz. This can be seen by writing $f \sim \langle P_r \rangle \tau_D / U_0$ and replacing the expression for the depletion time τ_D with that calculated in Sec. III. Importantly, both $\langle P_r \rangle$ and $\langle P_T \rangle$ scale like V_p^2 in the linear regime, which means that the fraction of laser energy converted to terahertz is independent of the pulse energy.

We may now estimate the amount of terahertz generated. The peak value of f in Fig. 6(c) is less than 1% . We note,

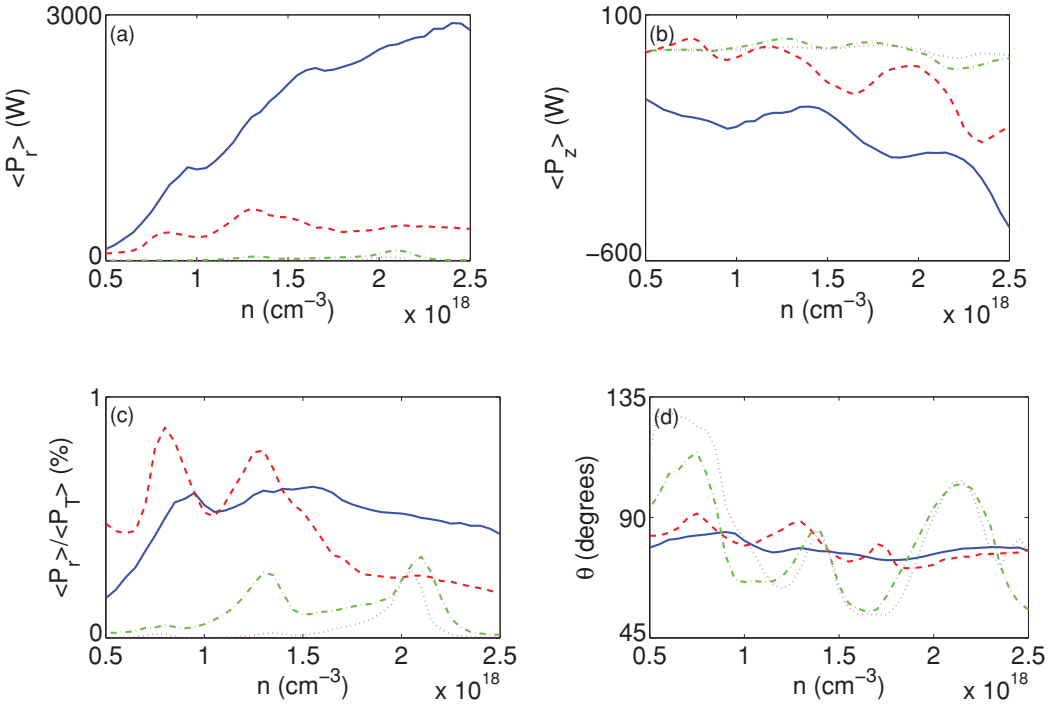

FIG. 6. (Color online) Plots involving various quantities as a function of density for channel widths $w_{ch} = 15\,\mu$m (blue, solid), $w_{ch} = 25\mu$m (red, dashed), $w_{ch} = 50\ \mu$m (green, dash-dot), and $w_{ch} = 75\ \mu$m (magenta, dotted). The quantities are (a) average power flow in the radial direction, (b) average power flow in the axial direction, (c) percentage of laser energy converted to terahertz, and (d) angle between the Poynting vector measured outside the channel and the axis.

however, that these results are from a system with artificially high collisional damping, which in these simulations is $\nu = 8c/L_S$, and so we expect the recorded conversion fraction is lower than that for a real channel. Extrapolation from a study of the variation of f with damping rate, along with crude estimates of the effect of damping [for example, multiplying f by $\exp(\nu r_0)$] suggest that at most, the presence of damping reduces f by a factor of two. The values of the pulse depletion length are displayed in Table II for different mode widths using a conversion fraction of $2f$. The depletion length was calculated for a $U_0 = 0.01$ J pulse and rescaled for a $U_0 = 0.5$ J pulse at a density of 1.3×10^{18} cm^{-3}, which corresponds to a peak in Fig. 6(c) for both small and large mode widths. The rescaling was accomplished using the fact that L_D scales like V_p^{-1}.

The results in Table II must be discussed in the context of the nonevolving pulse approximation, details of which are found in Sec. III. The depletion lengths calculated for the low-energy pulse are longer than the group velocity dispersion lengths, although the amount of terahertz produced is so low that this case is of little interest. The high- energy pulse produced sufficient terahertz to be of interest, although for small mode widths the plasma response is weakly relativistic ($a_0 = 0.8$ for the 15-μm case), and so the pulse evolution will not be represented accurately by Eq. (25).

TABLE II. Values of energy emitted in terahertz radiation and laser pulse depletion length for two different values of pulse energy and various mode widths. These quantities are calculated for a density of 1.3×10^{18} cm^{-3}, corresponding to peaks in Fig. 6(c).

	$U_0 = 0.01$ J		$U_0 = 0.5$ J	
w_{ch} (μm)	E_{THz} (mJ)	L_D (cm)	E_{THz} (mJ)	L_D (cm)
15	0.12	1000	6.1	22
25	0.15	3700	7.8	76
50	0.054	16 000	2.7	340
75	0.0034	37 000	0.17	780

During nonlinear pulse evolution in an axially uniform channel, however, the pulse initially compresses due to the reduction in plasma density behind the pulse. During this phase, the depletion rate increases. At later times the pulse lengthens and the depletion rate is reduced. Let us assume that the qualitative features of nonlinear pulse evolution in a corrugated channel are similar to those in an axially uniform channel. Then, since most of the pulse energy is depleted during the first phase of pulse evolution and the terahertz production rate is larger for stronger pulses, the values of L_D for the 0.5 J pulse serve as an upper bound for an effective depletion length, defined to be the length over which significant terahertz production occurs in a real channel. We note that some of the linear features of pulse evolution in a corrugated channel, such as the fact that the depletion length is longer than that given in Eq. (26) due to variation of plasma wavelength with density modulations, are already accounted for in the depletion estimates given in Table II.

An interesting feature of Fig. 6(c) is the presence of peaks in the value of f at different densities. There are two possible reasons for this density-dependent enhancement of terahertz output. The first reason is that the angle of the Poynting vector outside the channel is not always perpendicular to the axis, as

seen in Fig. 6(d). The reason for this will be discussed later in this section. The result is that $\langle P_r \rangle$ is enhanced when the measured angle is close to 90 degrees. Multiplying the data in Fig. 6(c) by the sine of the angles in Fig. 6(d) reveals, however, that this effect is minimal.

The second reason is related to enhanced coupling of the laser to terahertz modes at the so-called π and 2π points. These are the points on the dispersion curves at which $k/k_m = n$ and $k/k_m = 2n$, respectively. Antonsen *et al.* [14] discusses the importance of these special points in their treatment of the δ-function periodic profile. Of central importance in their calculation is a coupling constant that is proportional to the z average of the electric field divergence, i.e.,

$$I = \frac{1}{d}\int_0^d dz\, \nabla \cdot \boldsymbol{E}, \tag{31}$$

where $d = 2\pi/k_m$.

We may evaluate this for our density profile by assuming that the electric field divergence takes the form of a Floquet solution, as is found in Eq. (10). Adding this to its complex conjugate and integrating over one period of the structure yields

$$I = \sum_{\gamma=-\infty}^{\infty} \left(2\,\mathrm{Im}\{B_\gamma\}\frac{\cos(kd)-1}{(k-\gamma k_m)d} + 2\mathrm{Re}\{B_\gamma\}\frac{\sin(kd)}{(k-\gamma k_m)d}\right). \tag{32}$$

The π (2π) points occur when $kd = n\pi$ for odd (even) n. The second term in this sum is a maximum when $n = 2\gamma$, which only occurs at a particular 2π point and is zero for all other 2π points and all π points. Conversely, the first term is an extremum for all π points and vanishes for all 2π points. Because the dispersion curves, and hence the lightline intersections, shift with changing density, there are special densities at which the lightline intersects a dispersion curve at a π or 2π point. We can estimate the densities at which the coupling is maximum by combining the trigonometric functions in Eq. (32) with Eq. (13), which predicts the frequencies of generated terahertz modes. The results depend on the lightline intersection number, which must be determined by a frequency-space analysis of the system, and on the Fourier coefficients B_γ, which are not known. This makes it impossible to determine exactly the coupling as a function of density; however, for the first lightline intersection in a 50-μm channel, the 2π points occur at densities of 1.3×10^{18} and 2.2×10^{18} cm^{-3}, while the π points occur at densities of 8.5×10^{17} and 1.7×10^{18} cm^{-3}. Comparing these numbers to Fig. 6(c), we see that the enhanced terahertz output occurs at densities corresponding to 2π point intersections.

The results presented thus far have been for a fixed pulse length of 50 fs. For the purpose of optimizing terahertz production, it is useful to study the effects of pulse length on power output. Fig. 7 contains the results of a study conducted for pulse lengths ranging from 6 to 150 fs, again for a pulse energy of $U_0 = 0.01$ J, modulation amplitude $\delta = 0.9$, density cutoff parameters $r_c = 2w_{\mathrm{ch}}$ and $r_0 = 3w_{\mathrm{ch}}$, optical wavelength 800 nm, density modulation period 50 μm, and total system length 0.16 cm. The smaller system length is necessary because a larger resolution is required to resolve the shorter pulse lengths considered. Since we choose the damping to vary with inverse simulation length, the result of this change is to reduce the amount of terahertz radiation that escapes from the channel. Note that this reduction would not appear in an experimental result, in which the damping rate would be independent of simulation length.

The prominent feature of Fig. 7(a) is the decrease in power output with increasing pulse length over much of the domain, with a maximum at $\tau \simeq 12$ ps. The decrease occurs since the ponderomotive force is stronger for smaller pulse lengths, both because the gradient of V_p scales like $1/\tau$ and because the pulse energy is fixed, leading to a variable peak ponderomotive potential. In Fig. 7(b) we see the average power transferred from the laser pulse to the plasma. This is linear in the range 25–100 fs, with some deviation outside this range. This quantity varies with τ for the same reason as $\langle P_r \rangle$. The increase in the gradient of $\langle P_T \rangle$ at small pulse lengths occurs because the bandwidth of plasma excitations increases rapidly as $\tau \to 0$, and so more energy is transferred to plasma waves. The increase in energy going into plasma waves means that less is available for terahertz radiation, which explains the peak seen in (a) Publisher is John Wiley and Sons, 605 Third Avenue, New York NY 10158.

In Fig. 7(c) we see the ratio of $\langle P_r \rangle$ to $\langle P_T \rangle$, which we again interpret as the fraction of pulse energy that can be converted to terahertz radiation. As before, the combination of these two quantities results in a maximum, although this now occurs at $\tau \simeq 25$ ps. Thus, our previous choice of a 50-fs pulse did not result in the maximum terahertz generation. The final Fig. 7(d) contains the same results as (b), but rescaled so that the ponderomotive potential is fixed. The pulse energy is no longer constant, but its value for a 6-fs pulse is $U_0 = 0.01$ J. The purpose of this last plot is to verify that the results presented here are consistent with the fact that for fixed a_0, the maximum density perturbation occurs when the pulse duration matches the plasma period, which in this case is $\sim$100 fs.

Now we present recorded values of the average radial power flow per unit frequency. We begin by studying the effect of different cutoff radii on the terahertz output and then study the power spectrum as a function of density. The first set of results, seen in Fig. 8, are for channels with mode widths of $w_{\mathrm{ch}} = 15\mu$m and $w_{\mathrm{ch}} = 50$ μm, both with an on-axis mean density of $n_0 = 10^{18}$ cm^{-3}. The cutoff function is found in Eq. (3), and we consider $1.5w_{\mathrm{ch}} \leqslant r_c \leqslant 3.5w_{\mathrm{ch}}$ and $r_0 - r_c = w_{\mathrm{ch}}$. According to the discussion in Sec. II, different values of r_c will result in different numbers of quasibound modes in the channel. The pulse length is once more 50 fs, and the remaining parameters are the same as for previous results.

In Fig. 8(a) we see several different excitations. For $r_c = 1.5w_{\mathrm{ch}}$ (top), there should only be one bound mode in the system, and so the visible excitations correspond to several different Floquet modes of the fundamental radial eigenmode. These excitations are somewhat broader than those for larger cutoff radius because for small r_c, the mode loses energy through the channel wall more rapidly. There is therefore a damping rate associated with the measured modes, and broadening occurs. For larger values of r_c we see higher frequency excitations. We show later that the excitation at about 23 THz that appears for $r_c > 2.5w_{\mathrm{ch}}$ is a second-order

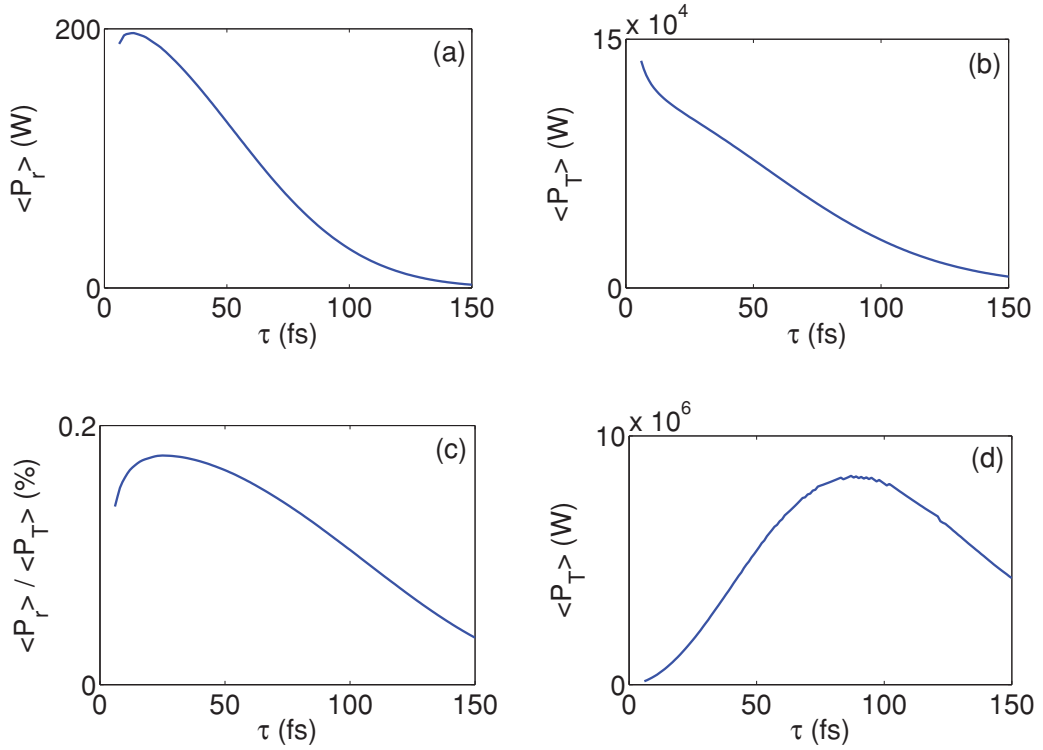

FIG. 7. (Color online) Plots involving various quantities as a function of pulse duration for density $n_0 = 1.25 \times 10^{18}$ cm^{-3} and channel width $w_{ch} = 25$ μm. The quantities are (a) average power flow in the radial direction, (b) average power transferred from the laser pulse to the plasma, (c) percentage of laser energy converted to terahertz and (d) average power transferred from the laser pulse to the plasma rescaled for fixed peak ponderomotive potential. Note that at $\tau = 50$ fs, these quantities do not match the results in Fig. 6 because the simulation length was shorter, and the damping rate ν was necessarily larger.

radial eigenmode. The appearance of second-order radial eigenmodes is consistent with the number of modes we expect the channel to support, as calculated from Eq. (17).

Fig. 8(b) shows a single peak at about 12 THz for small values of r_c and two peaks for larger cutoff radii. In this case, the frequency difference between successive Floquet modes is

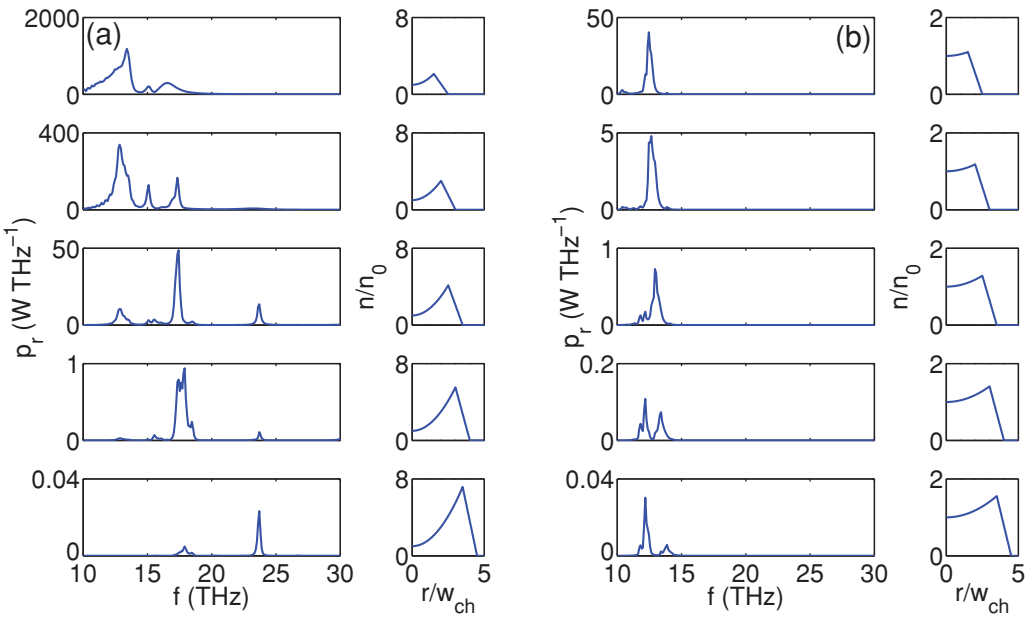

FIG. 8. (Color online) Average radial power spectral density for different cutoff radii and for corrugated channels with mode width (a) $w_{ch} = 15$ μm and (b) $w_{ch} = 50$ μm. The topmost plots have $r_c = 1.5w_{ch}$, and the cutoff radius increases by $0.5w_{ch}$ for each successive plot. The subfigure to the right of each power plot displays a z-averaged radial density profile.

at most 3 THz, while the frequency difference between (the same Floquet excitation of) successive radial eigenmodes is at most 0.6 THz. These frequency differences are less than in the case of a smaller channel, and so while the excitations occur at around the expected frequency, we cannot claim them to be modes of a particular type and index.

We may study the excitations we see here in more detail by looking at the z-t Fourier transform of a field quantity measured outside the channel. This result is shown for the case $r_c = 2w_{\rm ch}$ in Fig. 9, along with the lightline and a set of dispersion curves. We make this choice since this channel has one quasibound mode but may still leak a significant amount of radiation. We can easily identify in these plots the modes seen in Fig. 8. We see at each excited frequency several different axial wavenumbers. These different wavenumbers come from the different spatial harmonics that comprise the Floquet modes, and as such they are separated by k_m. In vacuum these correspond to electromagnetic waves with wave vectors that are oblique to the z axis. The angle of propagation may be calculated using $\omega = |\boldsymbol{k}|c$. We note that for $k_z c > \omega$, there are no spatial harmonics present. This is easily explained by considering the perpendicular wavenumber $k_\perp$, which outside the channel is given by

$$ck_\perp = \sqrt{\omega^2 - k_z^2 c^2}. \tag{33}$$

The perpendicular wavenumber is imaginary for $|k_z c| > \omega$, and so these spatial harmonics are evanescent outside the channel boundary. Harmonics outside the channel boundary that have $|k_z c| \leqslant \omega$ have a real perpendicular wavenumber and must therefore propagate away from the channel at an angle θ given by $\cos(\theta) = k_z c/\omega$. Since there are multiple spatial harmonics that satisfy the inequality for real $k_\perp$, we conclude that there will be a set of "scattering" angles associated with each channel and that the number of angles in this set will increase with density, increase with lightline intersection number, and decrease with mode width. These angles are given by

$$\theta = \arccos\left(1 - \frac{\beta k_m c}{\omega}\right) \qquad \beta = 0, 1, \ldots, \mathtt{int}(2\omega/k_m c). \tag{34}$$

The next set of results once again consists of values of the average radial power flow per unit frequency, this time recorded for a fixed value of $r_{\rm ch} = 2w_{\rm ch}$. This is done for mode widths of 15, 25, 50, and 75 μm, and densities ranging from 5×10^{17} cm^{-3} to 2.5×10^{18} cm^{-3}. The remaining parameters are the same as those used previously to generate Fig. 8.

In Fig. 10 we see the variation of frequency of side-coupled radiation with density. For comparison, we plot the frequencies predicted by the small δ theory for the first five Floquet modes associated with the fundamental and second radial eigenmodes of the channel.

The fit is surprisingly good given our choice of $\delta = 0.9$. We explain this by considering the perturbative "solution" to the Matthieu equation (i.e., assuming that coefficients A_α in Eq. (10) vanish for sufficiently large α). This solution yields a finite number of dispersion curves with approximate band gaps that range up to some maximum frequency and that are periodic in k out to some integer multiple of k_m. As we increase the perturbative order, the number of dispersion curves increases (increasing the range in ω), as does the number of periods in k over which they extend. Thus, since the excitations we observe come from the first few intersections of the lightline with the dispersion curves, which occur within the first few periods in k, a low-order perturbative approximation should give an accurate result, with predictions far from the band gaps being more accurate than those close to the band gaps.

The gradient (dn/df) of the line corresponding to the lowest-numbered Floquet mode is significantly different than other Floquet modes. We see in Fig. 10(a) that this follows the excitation corresponding to the 17-THz peak in the second plot of Fig. 8(a). (This figure corresponds to a line out of Fig. 10(a) at density $n = 10^{18}$ cm^{-3}.) Furthermore, the same line plotted for the second radial eigenmode is shifted to significantly higher frequency. Comparing this to the third line in Fig. 8(a) suggests that the 23-THz excitation here is a second-order radial eigenmode.

The general trend seen in Fig. 10(a) is for the power output to increase with density, which is consistent with the total power output results presented at the beginning of this section. The behavior is somewhat different for larger mode widths, however. For Fig. 10(b), the peak output occurs at 15 THz at a density of about 1.4×10^{18} cm^{-3} and at higher densities remains at a roughly constant level, albeit with a larger number of excitations. For Figs. 10(c) and 10(d) the peak output occurs at 18 THz at a density of about 2×10^{18} cm^{-3} in both cases, and is sufficiently pronounced that it is difficult to see any other excitations. Other excitations are present at a much lower level,

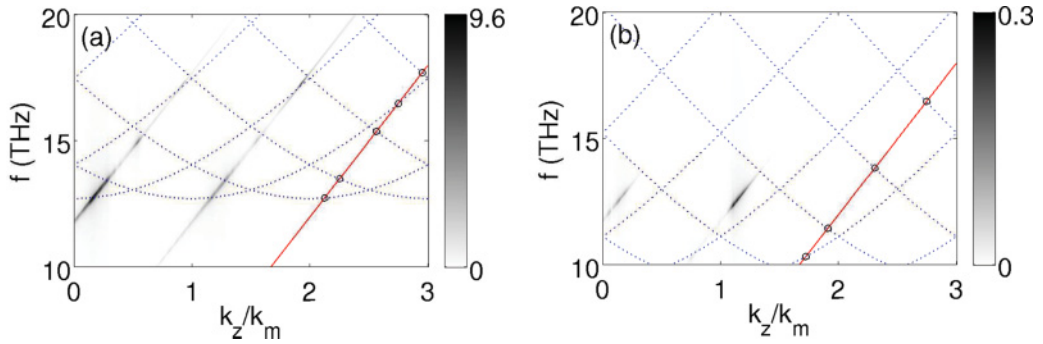

FIG. 9. (Color online) Two-dimensional Fourier transforms of E_z taken at fixed radius outside the channel for (a) $w_{\rm ch} = 15$ μm and (b) $w_{\rm ch} = 50$ μm. The red (solid) line is the lightline of the laser pulse, and the blue (dotted) curves are the functions in Eq. (12) that constitute the approximate dispersion relation.

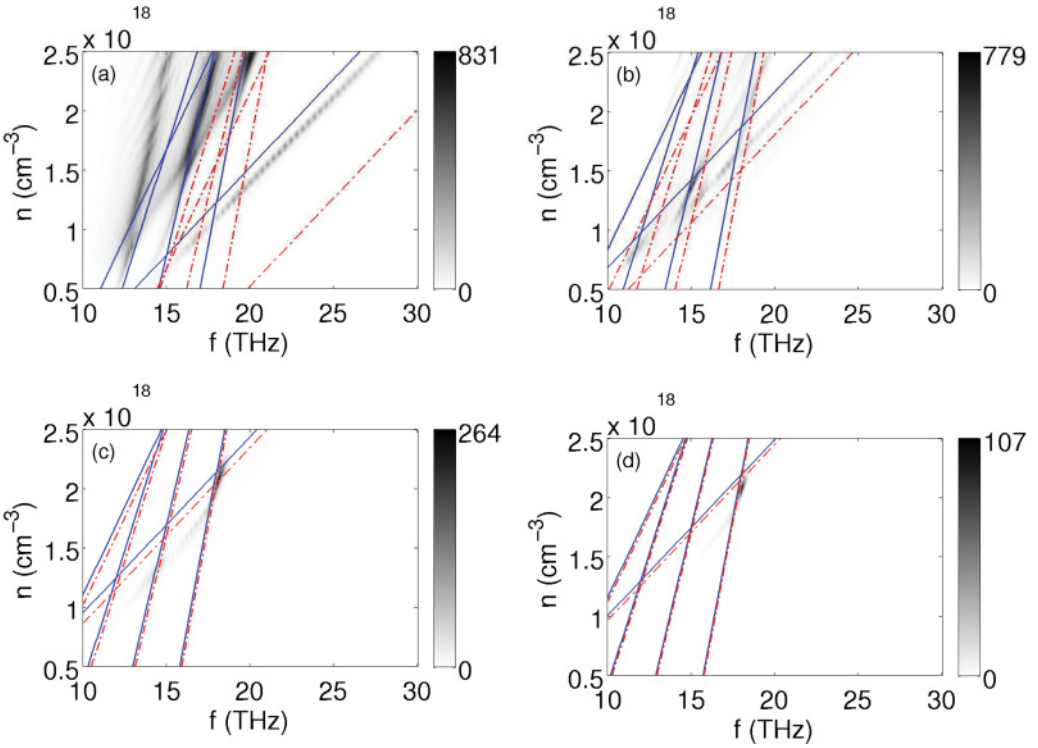

FIG. 10. (Color online) Plots of power density in frequency space as a function of density for channel widths (a) $w_{ch} = 15\ \mu$m, (b) $w_{ch} = 25\ \mu$m, (c) $w_{ch} = 50\ \mu$m, and (d) $w_{ch} = 75\ \mu$m. The orange (dashed) lines indicate the first five Floquet modes of the fundamental radial eigenmode, as predicted by the small δ theory.

as may be demonstrated with a plot of the logarithmic power output seen in Fig. 11.

In many cases the peak excitations in Fig. 10 occur at or near an intersection of two frequency prediction lines generated by Eq. (13). We explain this by noting that an intersection in Fig. 10 corresponds to an intersection of the lightline in a dispersion plot constructed with functions of the form given in Eq. (12) at a point where two of these functions themselves intersect. An intersection in Fig. 10 therefore corresponds to a π or a 2π point, and so we expect to see strong excitations at some of them.

The presence of a dominant excitation from a single lightline intersection for large mode widths, as opposed to many excitations for small mode widths, explains the features seen in Fig. 6(c) discussed at the beginning of this section. For large mode widths, there are densities at which the conversion fraction f is a maximum, and it was shown that for an $\alpha = 1$ lightline intersection, these densities correspond to 2π points. We now see, upon examination of Figs. 10(c) and 10(d), that this choice was justified. For smaller channels we see many excitations corresponding to different lightline intersection numbers, and each will have a different 2π point density. We expect that this will reduce the variation of the coupling with density and so there will not be a large variation with density in the conversion factor f. This is consistent with what is observed.

V. CONCLUSION

In conclusion, we have studied numerically the generation of terahertz radiation in a corrugated plasma channel. We have

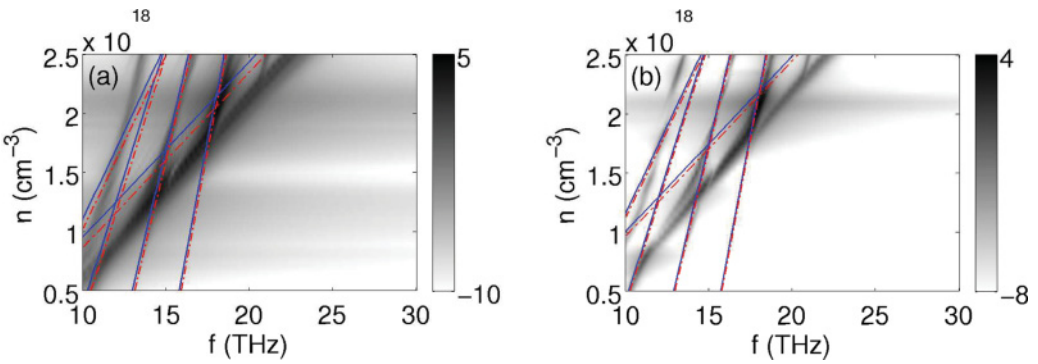

FIG. 11. (Color online) Log plots of power density in frequency space as a function of density for channel widths (a) $w_{ch} = 50\ \mu$m and (b) $w_{ch} = 75\ \mu$m. Comparing this with Fig. 10 verifies that the frequency predictions are accurate for large mode widths.

found that terahertz modes are indeed excited, the reason being that the laser pulse can phase-match with the slow-wave spatial harmonics supported by the channel. Some of these harmonics can then couple to free-space radiation modes on the side of the channel, with the angle of propagation being determined by the period in k_z in which the spatial harmonic wavenumber corresponding to the free space mode resides. Our results suggest that a significant fraction of the terahertz radiation power flow is radial, which is advantageous since these modes do not have to travel the length of the channel in order to escape. We have not completely discounted the possibility of axial terahertz extraction, however. We have also found that a small-density-modulation-amplitude approximation predicts terahertz radiation at frequencies similar to those observed in simulation results, despite the fact that the simulations were run with large modulation amplitudes.

We have found that the total radial power output is larger for smaller mode widths and for higher densities. The variation with mode width occurs because smaller mode widths lead to larger gradients of the ponderomotive potential, and because for fixed pulse energy, the peak ponderomotive potential increases with decreasing w_{ch}. The power output is larger for higher densities because the laser pulse drives larger currents and so does more work. We have found that terahertz is strongly emitted at certain angles corresponding to the axial wavenumbers of the different spatial harmonics, and we have found variation in power output with density due to the presence of π and 2π points in the dispersion relation. An experiment should therefore target the "special" densities at which enhanced coupling occurs.

Finally, we have estimated the total fraction of laser pulse energy that is converted into terahertz to be around 1% for the densities and mode widths we considered. We have also shown for one set of channel parameters that the 50-fs pulse length is not optimum for generating terahertz and that the ideal pulse is somewhat shorter. It appears, however, that this will not increase the pulse energy conversion fraction significantly. Extrapolating our results into the nonlinear regime, we obtain 6 mJ of terahertz from a 0.5 J pulse, with a linear depletion length of approximately 20 cm. This depletion length is for a 15-μm matched spot, and it increases significantly with spot size. Given the experimental constraints and the fact that the estimated terahertz power output assumes total pump depletion, we find that terahertz production requires small spot sizes.

A 0.5 J, 15-μm pulse has a normalized amplitude of $a_0 = 0.8$, and so pump depletion will proceed in the weakly relativistic regime. Therefore we treat the estimated depletion length as the upper bound to an effective depletion length over which most of the terahertz would be produced in a real system. The general conclusion is that a small-spot, short pump pulse containing a significant fraction of a Joule, and a corrugated channel of several centimeters, is required to produce millijoule-level amounts of terahertz radiation. Simulating such a system requires a nonlinear and relativistic analysis of pulse evolution in a corrugated plasma channel.

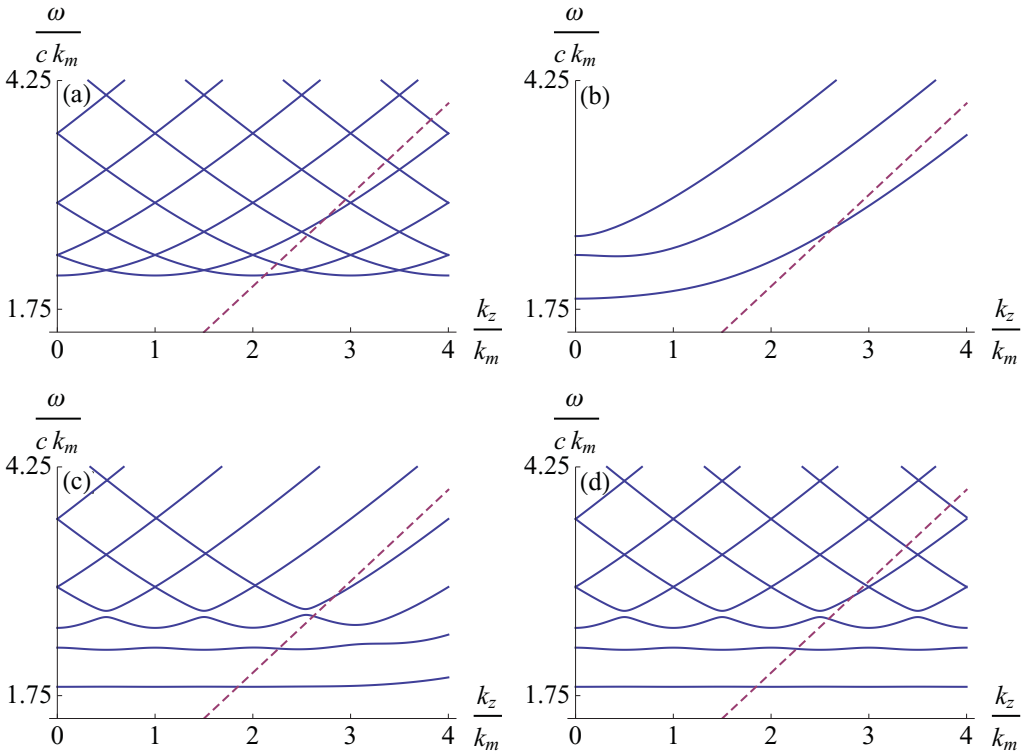

FIG. 12. (Color online) Dispersion curves (blue, dotted) generated by evaluating a finite-sized version of the determinant shown in Eq. (A1). Fig. (a) contains the dispersion construction discussed in Sec. II, which is the dispersion relation from a single-element determinant reproduced many times. The remaining figures contain dispersion curves calculated for (b) 3, (c) 9, and (d) 15 nonzero Fourier coefficients. The lightline (red, solid) is displayed also.

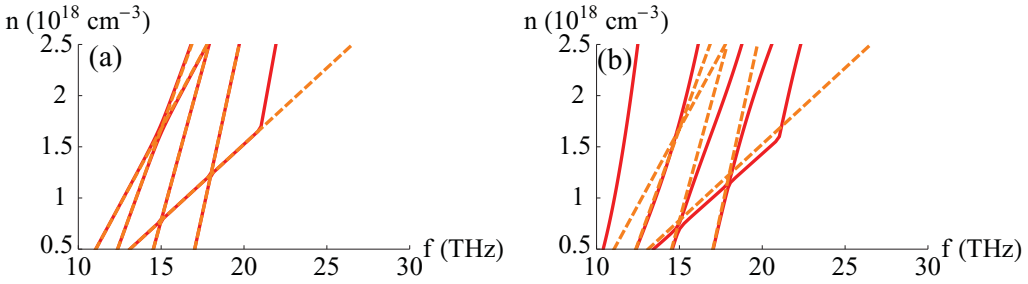

FIG. 13. (Color online) Frequencies of lightline intersections with the dispersion curves in Fig. 12(a) (orange, dashed) and Fig. 12(b) (red, solid) for (a) $\delta = 0.05$ and (b) $\delta = 0.9$.

ACKNOWLEDGMENTS

This work was supported by the Office of Naval Research and the US Department of Energy.

APPENDIX: CALCULATING THE APPROXIMATE DISPERSION RELATION

In calculating the mode structure in a corrugated plasma waveguide in Sec. II, we encounter a one-dimensional ODE [Eq. (9)] which is related to the Matthieu equation. We construct a dispersion relation in the $\delta \to 0$ limit by superimposing the dispersion curves for all of the different spatial harmonics of the solution, found in Eq. (10). This dispersion relation possesses the correct periodicity but is somewhat inaccurate near the band gaps. We note, however, that the results obtained from simulations in the $\delta \to 1$ limit match to some degree the approximate dispersion relation. The purpose of this Appendix is to understand this result and to quantify the differences between our dispersion relation and the exact result.

We begin by writing Eq. (11) in matrix form. The result is a vanishing product of a tridiagonal matrix and a vector of Fourier coefficients, i.e., $\mathsf{M} \cdot \boldsymbol{A} = 0$. Defining for brevity $\Omega_\alpha^2 = k_0^2 c^2 - (k_z - \alpha k_m)^2 c^2$, the dispersion relation (which is the condition for the existence of a nontrivial solution) is given by

$$\det(\mathsf{M}) = \begin{vmatrix} \ddots & \ddots & & & 0 \\ \ddots & 2\Omega_{\alpha-1}^2 & -i\omega_{p0}^2\delta & & \\ & i\omega_{p0}^2\delta & 2\Omega_\alpha^2 & -i\omega_{p0}^2\delta & \\ & & i\omega_{p0}^2\delta & 2\Omega_{\alpha+1}^2 & \ddots \\ 0 & & & \ddots & \ddots \end{vmatrix} = 0. \quad \text{(A1)}$$

We proceed by considering the strength of the coupling between Fourier coefficients A_α. For neighboring coefficients, we write this schematically as $A_\alpha \sim \epsilon A_{\alpha\pm1}$, and thus $A_\alpha \sim \epsilon^N A_{\alpha\pm N}$. If ϵ is small, we may choose to keep terms only to order ϵ^N; hence a particular Fourier coefficient will only be coupled to $2N$ of its neighbors, after which it will be decoupled. Because of this decoupling, our product $\mathsf{M} \cdot \boldsymbol{A}$ of an infinitely extended matrix and vector will reduce to an infinite number of products of a $(2N+1) \times (2N+1)$ matrix with a vector.

We need only evaluate the determinant of one of these matrices, since the dispersion curves resulting from the determinant centered around α will be related to those from the determinant centered around $\alpha + 1$ by a translation of k_m. We note that this is exactly the procedure used to calculate the dispersion relation in Sec. II, where we kept terms to order ϵ^0 and thus evaluated a 1×1 determinant.

In general, the small parameter ϵ depends on both δ, the modulation wavenumber k_m, and the frequency and wavenumber associated with the region of interest in the dispersion relation. Since we are interested in the region surrounding the first few lightline intersections, we have $\epsilon \sim \omega_{p0}^2\delta/\omega_c^2$. We may estimate the required size of the determinant using $2N + 1 \sim 2\ln(\tau)/\ln(\epsilon) + 1$, where τ is the desired fractional contribution of the most distantly coupled Fourier coefficient. For $\tau = 0.01$, we have for a $\delta = 0.9$, $n = 10^{18}$ cm^{-3}, $w_{\rm ch} = 15\mu$m channel a required determinant size of $2N + 1 \sim 13$.

In Fig. 12 we see dispersion curves plotted for $n = 10^{18}$ cm^{-3}, $\delta = 0.9$, and $w_{\rm ch} = 15\ \mu$m for various determinant sizes, including $N = 1$. In the $N = 1$ graph, we plot multiple dispersion curves to show a full dispersion relation; however, for larger sizes we plot only the solutions from a single determinant centered around $\alpha = 0$. We observe that as the number of nonzero Fourier coefficients increases, the number of individual curves increases, as does their extent in k_z space. We note, however, that the curve structure and band-gap size for small ω and k_z is accurate for much smaller truncation values than are necessary for correct curve structure at large ω and k_z.

We also note that the curve structure at large frequency very closely matches the piecewise dispersion relation, which explains why our simulation results conform so closely. For the case $\delta = 0.05$ (not shown), the large band gaps that appear at low frequencies in the above plots reduce significantly, and the dispersion curves match the piecewise dispersion relation at low frequencies also.

Finally, we compare the frequencies generated by calculating the lightline intersections for the same density range as used in the simulations. These results are seen in Fig. 13 and should be compared to the simulation results in Fig. 10(a).

[1] A. Crocker, Nature **201**, 250 (1964).
[2] J. Faist, F. Capasso, D. L. Sivco, C. Sirtori, A. L. Hutchinson, and A. Y. Cho, Science **264**, 553 (1994), [http://www.sciencemag.org/cgi/reprint/264/5158/553.pdf], [http://www.sciencemag.org/cgi/content/abstract/264/5158/553].
[3] D. H. Auston, K. P. Cheung, J. A. Valdmanis, and D. A. Kleinman, Phys. Rev. Lett. **53**, 1555 (1984).
[4] C. Fattinger and D. Grischkowsky, Appl. Phys. Lett. **54**, 490 (1989), [http://link.aip.org/link/?APL/54/490/1].
[5] Z. Jiang and X.-C. Zhang, IEEE Trans. Microwave Theory Tech. **47**, 2644 (1999).
[6] A. Staprans, E. McCune, and J. Ruetz, Proc. IEEE **61**, 299 (1973).
[7] S. H. Gold and G. S. Nusinovich, Rev. Sci. Instrum. **68**, 3945 (1997), [http://link.aip.org/link/?RSI/68/3945/1].
[8] G. Ramian, Nucl. Instrum. Methods Phys. Res. A **318**, 225 (1992), [http://www.sciencedirect.com/science/article/B6TJM-47434VR-1M/2/d59422963e466d210e1f1f95cac47a1c].
[9] K. W. Berryman, E. R. Crosson, K. N. Ricci, and T. I. Smith, Nucl. Instrum. Methods Phys. Res. A **375**, 526 (1996), *Proceedings of the 17th International Free Electron Laser Conference*, [http://www.sciencedirect.com/science/article/B6TJM-3VSPXXG-6Y/2/0ffc38c5cf17797de08e6424666bc2a6].
[10] V. Bolotin *et al.*, Nucl. Instrum. Methods Phys. Res. A **543**, 81 (2005), *Proceedings of the XV International Synchrotron Radiation Conference*, [http://www.sciencedirect.com/science/article/B6TJM-4FDMVSN-C/2/b5cd970855d8eed7c1e7796ca99948e6].
[11] W. P. Leemans *et al.*, Phys. Rev. Lett. **91**, 074802 (2003).
[12] H. Hamster, A. Sullivan, S. Gordon, W. White, and R. W. Falcone, Phys. Rev. Lett. **71**, 2725 (1993).
[13] J. Yoshii, C. H. Lai, T. Katsouleas, C. Joshi, and W. B. Mori, Phys. Rev. Lett. **79**, 4194 (1997).
[14] T. M. Antonsen, J. Palastro, and H. M. Milchberg, Phys. Plasmas **14**, 033107 (2007), [http://link.aip.org/link/?PHP/14/033107/1].
[15] B. D. Layer, A. York, T. M. Antonsen, S. Varma, Y.-H. Chen, and H. M. Milchberg, Phys. Rev. Lett. **99**, 035001 (2007).
[16] J. P. Palastro, T. M. Antonsen, S. Morshed, A. G. York, and H. M. Milchberg, Phys. Rev. E **77**, 036405 (2008).
[17] B. A. Shadwick, C. B. Schroeder, and E. Esarey, Phys. Plasmas **16**, 056704 (2009), [http://link.aip.org/link/?PHP/16/056704/1].
[18] A. Ting, E. Esarey, and P. Sprangle, Phys. Fluids B: Plasma **2**, 1390 (1990), [http://link.aip.org/link/?PFB/2/1390/1].
[19] J. D. Jackson, *Classical Electrodynamics*, 3rd ed. (John Wiley and Sons, New York, 1998).
[20] P. Mora and T. M. Antonsen, Phys. Plasmas **4**, 217 (1997), [http://link.aip.org/link/?PHP/4/217/1].
[21] NVidia, "CUDA GPUs," [http://www.nvidia.com/object/cuda_gpus.html].